ADVANCED MATERIALS
www.advmat.de

Atomically Dispersed Dual-Site Cathode with a Record High Sulfur Mass Loading for High-Performance Room-Temperature Sodium–Sulfur Batteries

Bin-Wei Zhang, Liuyue Cao, Cheng Tang, Chunhui Tan, Ningyan Cheng, Wei-Hong Lai, Yun-Xiao Wang, Zhen-Xiang Cheng, Juncai Dong, Yuan Kong,* Shi-Xue Dou, and Shenlong Zhao**

Room-temperature sodium–sulfur (RT-Na/S) batteries possess high potential for grid-scale stationary energy storage due to their low cost and high energy density. However, the issues arising from the low S mass loading and poor cycling stability caused by the shuttle effect of polysulfides seriously limit their operating capacity and cycling capability. Herein, sulfur-doped graphene frameworks supporting atomically dispersed 2H-MoS_2 and Mo_1 (S@MoS_2-Mo_1/SGF) with a record high sulfur mass loading of 80.9 wt.% are synthesized as an integrated dual active sites cathode for RT-Na/S batteries. Impressively, the as-prepared S@MoS_2-Mo_1/SGF display unprecedented cyclic stability with a high initial capacity of 1017 mAh g^{-1} at 0.1 A g^{-1} and a low-capacity fading rate of 0.05% per cycle over 1000 cycles. Experimental and computational results including X-ray absorption spectroscopy, in situ synchrotron X-ray diffraction and density-functional theory calculations reveal that atomic-level Mo in this integrated dual-active-site forms a delocalized electron system, which could improve the reactivity of sulfur and reaction reversibility of S and Na, greatly alleviating the shuttle effect. The findings not only provide an effective strategy to fabricate high-performance dual-site cathodes, but also deepen the understanding of their enhancement mechanisms at an atomic level.

1. Introduction

Sulfur is an attractive electrode material for next-generation battery systems because of its abundant resources and high theoretical capacity (1672 mAh g^{-1}).[1] In general, electrochemical reduction of sulfur in alkaline metal-sulfur batteries is a 16-electron transfer process, involving a solid-liquid transition from S_8 ring molecules to long-chain polysulfides and then short-chain sulfides.[2] However, its sluggish conversion kinetics and polysulfide shuttling effects lead to low capacity and fast capacity fade, which results in low energy and power densities in practical operation.[3] In addition, the insulating nature of sulfur will aggravate the sluggish reactivity of conversion. Room-temperature sodium–sulfur (RT-Na/S) batteries are one of the most promising systems for low-cost and high energy densities due

B.-W. Zhang
School of Chemistry and Chemical Engineering
Chongqing University
Chongqing 400044, P. R. China
E-mail: binwei@cqu.edu.cn

B.-W. Zhang
Center of Advanced Energy Technology and Electrochemistry
Institute of Advanced Interdisciplinary Studies
Chongqing University
Chongqing 400044, P. R. China

B.-W. Zhang, N. Cheng, W.-H. Lai, Y.-X. Wang, Z.-X. Cheng, S.-X. Dou
Institute for Superconducting and Electronic Materials
Australian Institute of Innovative Materials
University of Wollongong
Innovation Campus, SquiresWay, North Wollongong
New South Wales 2500, Australia

The ORCID identification number(s) for the author(s) of this article can be found under https://doi.org/10.1002/adma.202206828.

DOI: 10.1002/adma.202206828

L. Cao, C. Tan, S. Zhao
The University of Sydney
School of Chemical and Biomolecular Engineering
Sydney, New South Wales 2006, Australia
E-mail: shenlong.zhao@sydney.edu.au

C. Tang, C. Tan
School of Chemical Engineering
The University of Adelaide
Adelaide, South Australia 5005, Australia

J. Dong
Beijing Synchrotron Radiation Facility
Institute of High Energy Physics
Chinese Academy of Sciences
Beijing 100049, P. R. China

Y. Kong
Hefei National Laboratory for Physical Sciences at the Microscale
Synergetic Innovation Center of Quantum Information and Quantum Physics
University of Science and Technology of China
Hefei 230026, P. R. China
E-mail: kongyuan@ustc.edu.cn

to the abundance and high theoretical capacity both of sodium and sulfur.[4] Nevertheless, RT-Na/S batteries suffer from several challenges, such as the insulating nature of sulfur and fast capacity fade.[5] The sluggish reactivity of S and the shuttling effect of polysulfides are responsible for rapid capacity fading, while the incomplete reduction of polysulfide intermediates rather than Na_2S leads to a low accessible capacity.[6] Besides these effects, the low loading amount of sulfur active material (currently reported S contents are lower than 60%) in the cathode still cannot satisfy the requirements of practical applications.[7] Therefore, the rational design of S hosts with high sulfur mass loading and efficient conversion kinetics is a crucial requisite for the development of practical RT-Na/S batteries.

Extensive efforts have been devoted to addressing the above mentioned drawbacks, most of which are focused on constructing S cathode materials by confining the sulfur species within carbon materials,[8] sulfides,[9] and metal electrocatalysts.[10] Among these, metal sulfide-based electrocatalysts with dual active sites have attracted increasing attention due to their advantages in trapping polysulfides for conversion into Na_2S and alleviating the 'shuttle effect'.[11] However, most reported dual active site electrocatalysts are created on bulk materials, nanoparticles, or aggregations, with limited capacity and conversion kinetics of sodium polysulfides.[12] Theoretically, atomically-dispersed dual site catalysts are the ideal candidates for high-performance sulfur cathodes because of their unique electronic structure, active atomic centers, and low coordination environment.[13] For instance, atomically-dispersed dual site cathodes possess maximal atom utilization, which can provide more accessible sites for sulfur and active site combinations. The redistribution of atomic orbital or synergistic effects will be further enhanced in atomic-level dual-site systems, which facilitates the formation of molecular bonding between atomic-level multi-active sites and intermediates, thereby decreasing the decomposition energy of polysulfides and improving the available sulfur mass loading.[14]

In this work, we first synthesized sulfur-doped graphene frameworks that support atomically dispersed 2H-MoS_2 and Mo_1 (S@MoS_2-Mo_1/SGF) with a record high S mass loading of 80.9% for RT-Na/S batteries. Remarkably, the S@MoS_2-Mo_1/SGF delivers an initial capacity of 1017 mAh g^{-1} and retains a high capacity of 505 mAh g^{-1} after 1000 cycles at 0.1 A g^{-1}. The enhanced mechanism of the atomic-level dual-active-site cathode was investigated by combining the operando X-ray technique with computational analysis. It is revealed that the atomically-dispersed dual site system can generate an unexpected delocalized electron effect that optimizes the electronic structure of active Mo, leading to a negative adsorption energy for sodium intermediates. Also, it is beneficial to promote the conversion kinetics of sodium polysulfides, thereby inhibiting the shuttle effect.

2. Results and Discussions

2.1. Atomic-Level Dual-Active Sites Wreathed on Sulfur-Doped Graphene Frameworks

Scheme S1 shows the synthesis process of S@MoS_2-Mo_1/SGF via a facile sulfur molecular vapor. Transmission electron microscope (TEM) images of S@MoS_2-Mo_1/SGF (**Figure 1**a) indicate that the structure of the graphene framework is well-maintained after loading sulfur. High-angle annular dark-field (HAADF) scanning transmission electron microscope (STEM) was employed to confirm that there were no obvious nanoclusters or nanoparticles on the surface of Mo_1/SGF and S@Mo_1/SGF (Figures S1 and S2, Supporting Information). Interestingly, both MoS_2 monolayer nanoclusters and single Mo

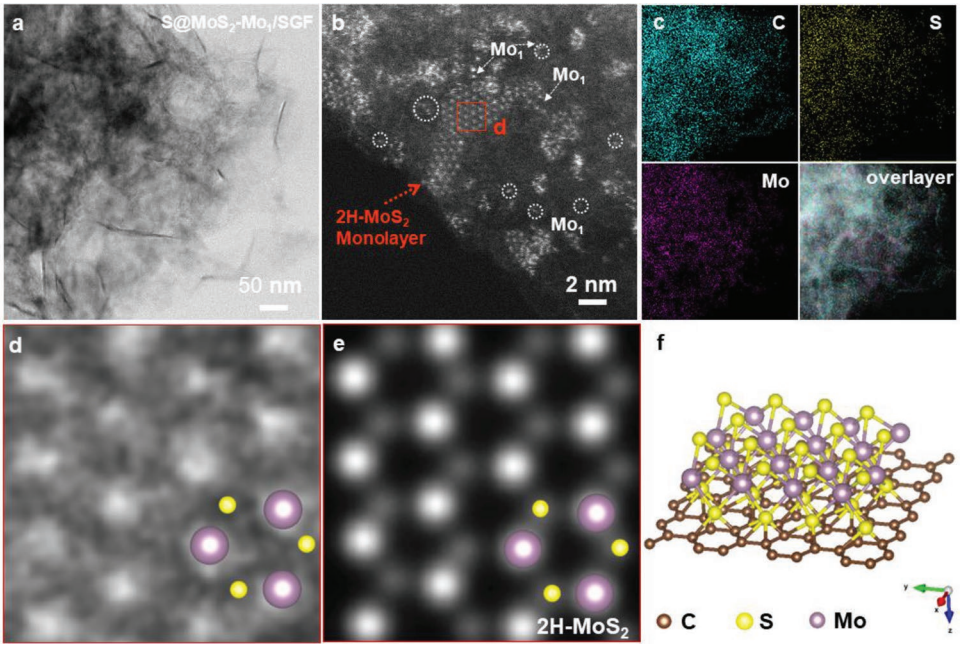

Figure 1. Electron microscopy images. a–c) TEM, HAADF-STEM images, and corresponding elemental mapping images of S@MoS_2-Mo_1/SGF. d–f) HR-STEM view and QSTEM model corresponding with a schematic illustration of 2H-MoS_2 monolayer structure.

atoms anchored on the surface of the SGF can be observed in the HAADF-STEM images of S@MoS_2-Mo_1/SGF (Figure 1b; Figure S3, Supporting Information). The elemental mapping images (Figure 1c) suggest that the obtained S@MoS_2-Mo_1/SGF is composed of C, S, and Mo without other impurities, with uniform dispersion of C, S, and Mo on the entire surfaces. To investigate the MoS_2 monolayer structure, high-resolution STEM (HR-STEM) images and quantitative STEM (QSTEM) simulations were employed (Figure 1d,e). According to STEM's Z-contrast principle (i.e., the image contrast I ~ atomic number $Z^{1.6\text{-}2.0}$), bright and dim represent Mo and S atoms, respectively.[15] The HAADF-STEM images (Figure 1d) reveal that the atomic structure of these clusters on the graphene is a typical hexagonal structure along the [001] zone axis. The model of S@MoS_2-Mo_1/SGF (Figure 1f) is identified by simulating the atomic resolution HAADF-STEM image (Figure 1e) via QSTEM software. In addition, the nearest and next-to-nearest distance between two metal atoms is 2.7 Å, which is in good agreement with the theoretical values (2.7 Å) of single-layer MoS_2 with 24 Mo atoms.[16] It can be concluded that Mo and S involved in reactions are distributed uniformly on the surface of graphene and grow in the form of a single-layer hexagonal MoS_2. The massive statistical data from the aberration-corrected STEM (Figure S3, Supporting Information) suggests that the average size of the 2H-MoS_2 monolayer clusters is ≈1.2 nm, which is consistent with the results in Figure S4 (Supporting Information). These experimental results combined with the simulation data confirm that S@MoS_2-Mo_1/SGF was successfully synthesized. For comparison, the MoS_2 monolayer clusters anchored on SGF (S@MoS_2/SGF) and sulfur-loaded plain SGF (S@SGF) were synthesized and the HAADF/HR-STEM images of S@MoS_2/SGF and S@SGF are shown in Figures S5 and S6 (Supporting Information). HAADF-STEM and elemental mapping images of S@SGF (Figure S6, Supporting Information) indicate that sulfur is well-distributed on the SGF without sulfur agglomeration.

X-ray absorption near-edge structure (XANES) and extended X-ray absorption fine structure (EXAFS) measurements (**Figure 2**a,b; Figure S7, Supporting Information) were used to study the coordination environment and electronic structure of S@MoS_2-Mo_1/SGF. The Mo K edge of Mo_1/SGF, S@Mo_1/SGF, and S@MoS_2-Mo_1/SGF shifts to higher energy compared with S@MoS_2/SGF, and standard Mo foil and MoS_2, indicating the chemical valence of Mo is higher than the standard MoS_2 and Mo foil.[14b] The higher Mo chemical valence of S@MoS_2-Mo_1/SGF could be attributed to the formation of the dual-site MoS_2-Mo_1 system, which facilitates the electron transfer from Mo to the loaded S. Additionally, XANES of S@MoS_2/SGF with 24 h thermal treatment is close to that of MoS_2 standard, which is relevant to the formation of assembled MoS_2. EXAFS results for Mo_1/SGF and S@MoS_2-Mo_1/SGF (Figure 2b) suggest that Mo_1/SGF possesses one main spacing ≈1.1 Å and the absence of Mo–Mo at 2.4 Å could be attributed to the presence of single Mo atoms, which is in agreement with the previous work.[17] Similarly, there is one peak in the EXAFS of S@MoS_2-Mo_1/SGF, suggesting the presence of single Mo atoms in S@MoS_2-Mo_1/SGF.[18] Interestingly, a peak appears at 2.65 Å in the EXAFS of S@MoS_2-Mo_1/SGF, which is a value midway between the spacings of the Mo–Mo bond in Mo foil (2.49 Å) and Mo–S bonds (2.87 Å) in MoS_2. Considering the presence of mono-layered MoS_2 in the S@MoS_2-Mo_1/SGF, it should be originated from the negative shift of the Mo–S bond, which

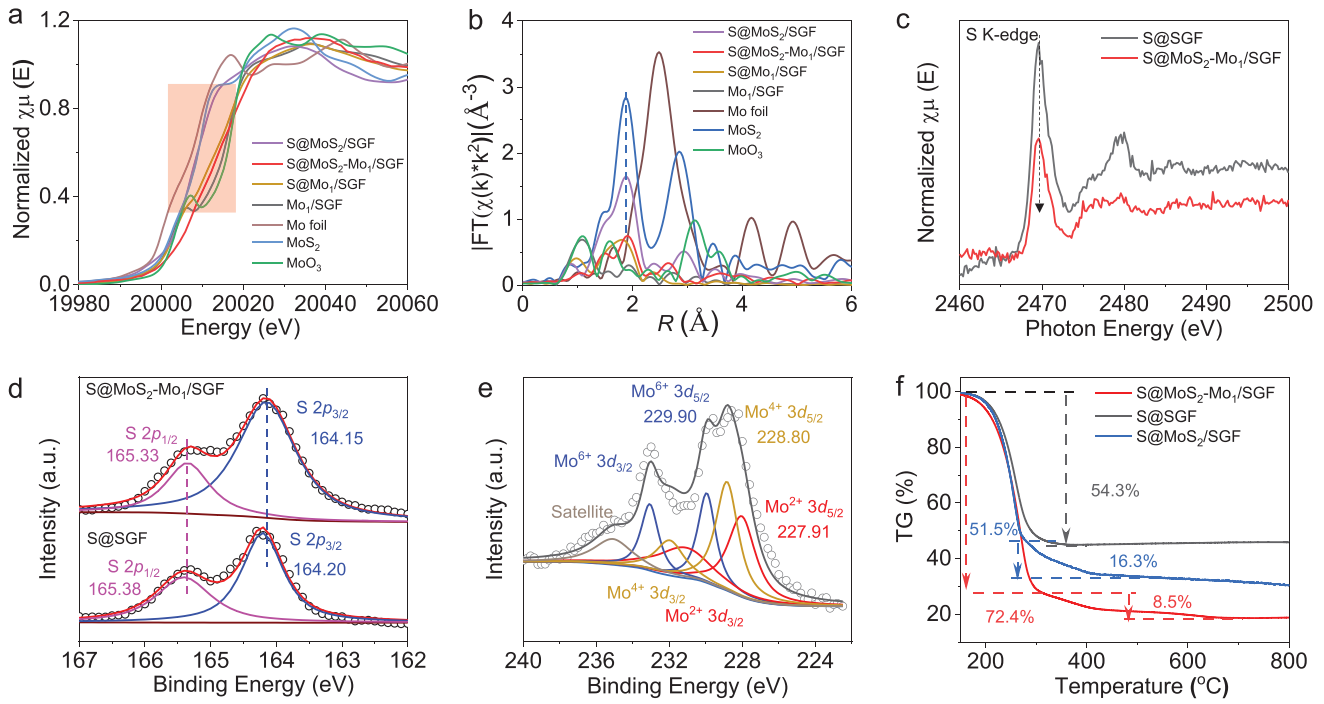

Figure 2. Characterizations of S@MoS_2-Mo_1/SGF. a) Mo *K*-edge XANES spectra and b) R-space EXAFS spectra of S@MoS_2-Mo_1/SGF, S@MoS_2/SGF, S@Mo_1/SGF, Mo_1/SGF, Mo foil, MoS_2, and MoO_3. c) S K-edge NEXAFS spectra, d) and e) XPS results of S@MoS_2-Mo_1/SGF and S@SGF. f) TGA results of S@MoS_2-Mo_1/SGF, S@MoS_2/SGF and S@SGF.

is consistent with the STEM and XANES results. As shown in Figure 1b, monolayered MoS_2 clusters are surrounded by single Mo atoms. This short range creates delocalized electron interfaces between monolayered MoS_2 and Mo_1, leading to an electron transfer from Mo to S.[19] This is the reason why the chemical valence of Mo in S@MoS_2-Mo_1/SGF is higher than in S@MoS_2/SGF. It is well-established that the electronic configuration has a close relationship with the geometric structure and bond distances.[20] In general, the higher the chemical valence of Mo components, the shorter the bond length. The relatively regular peak at 2.65 Å should be ascribed to the Mo–S in S@MoS_2-Mo_1/SGF. Different from the S@MoS_2-Mo_1/SGF, the EXAFS results for S@MoS_2/SGF present two intense peaks at 1.90 and 2.86 Å. Compared with the EXAFS of standard MoS_2, it can be seen that the two intense peaks should be attributed to the Mo–S bond in MoS_2. Therefore, EXAFS results demonstrate that the single Mo atoms can be assembled into MoS_2 more completely after longer thermal treatment.

Near-edge X-ray absorption fine structure (NEXAFS) spectra of S@MoS_2-Mo_1/SGF and S@SGF (Figure 2c; Figure S8, Supporting Information) were collected to study the electron transfer of sulfur. It can be seen that the S K-edge intensity in NEXAFS of S@MoS_2-Mo_1/SGF decreases compared with S@SGF, while the C K-edge intensity increases, verifying the electron transfer from MoS_2-Mo_1/SGF to S.[21] The transferring electrons will activate sulfur and enhance its reactivity and the kinetics of the formation of polysulfides. X-ray photoelectron spectroscopy (XPS) was employed to further investigate the chemical states in the samples (Figure 2d,e; Figure S9, Supporting Information). Figure 2d shows the S $2p_{3/2}$ peak (164.15 eV) of S@MoS_2-Mo_1/SGF (Figure 2d) negatively shifted by 0.05 eV compared with S@SGF (164.20 eV), which suggests that S is an electron acceptor. The XPS spectra in Figure 2e indicate the chemical valence of Mo consists of +2, +4, and +6. The various Mo^{2+} $3d_{5/2}$ (227.91 eV), Mo^{4+} $3d_{5/2}$ (228.80 eV), and Mo^{6+} $3d_{5/2}$ (229.90 eV) sub-spectra can be observed in the spectrum of S@MoS_2-Mo_1/SGF, which is attributed to the delocalized electron effect between MoS_2 and atomic Mo_1. Moreover, compared with that of pure MoS_2 (229.60 eV), Mo^{4+} $3d_{5/2}$ for S@MoS_2-Mo_1/SGF shows a 0.8 eV left-shift, which suggests the electron transfer from the delocalized electron system to S.[22] Thermogravimetric analysis (TGA) measurements (Figure 2f; Figure S10, Supporting Information) indicate that the S content stored in the mesoporous of S@MoS_2-Mo_1/SGF is 80.9 wt.%, higher than S@MoS_2/SGF (67.8 wt.%) and S@SGF (54.3 wt.%). Interestingly enough, there are two types of sulfur with different sublimation points in S@MoS_2-Mo_1/SGF. The amount of sulfur with a sublimation point below 320 °C in S@MoS_2-Mo_1/SGF was 72.4 wt.%, which is assigned to the sulfur occupying SGF porous. This is a much higher proportion than in S@MoS_2/SGF (51.5 wt.%) or S@SGF (54.3 wt.%). The sulfur with a higher sublimation point (>320 °C) in S@MoS_2-Mo_1/SGF amounted to 8.5 wt.%, demonstrating there is adsorbed sulfur on the surface of MoS_2-Mo_1. Notably, the total sulfur mass loading in the as-prepared S@MoS_2-Mo_1/SGF cathode is higher than that of all other reported cathode materials for RT-Na/S batteries (see Table S1, Supporting Information). The X-ray diffraction (XRD) results (Figure S11, Supporting Information) also indicate that sulfur is the main constituent for S@MoS_2-Mo_1/SGF, S@MoS_2/SGF, and S@SGF samples. In addition, no typical MoS_2 peak can be observed in the XRD pattern of S@MoS_2-Mo_1/SGF and S@MoS_2/SGF, indicating that the size of monolayer 2H-MoS_2 clusters is ultra-small.

2.2. Electrochemical Performance of Room Temperature Sodium–Sulfur Batteries

The discharge/charge profiles of the 1st, 2nd, 5th, and 10th cycles at 0.1 A g^{-1} for S@MoS_2-Mo_1/SGF, S@MoS_2/SGF, S@Mo_1/SGF, and S@SGF are presented in **Figure 3**a,b, Figures S12, and S13 (Supporting Information). The RT-Na/S@MoS_2-Mo_1/SGF cells during discharge display two plateaus from 2.20 to 2.02 V, and from 1.35 to 0.80 V, which corresponds to the formation of polysulfides and further sodiation into short-chain sulfides. The S@MoS_2/SGF and S@SGF also presented two plateaus. S@MoS_2-Mo_1/SGF samples displayed the highest initial capacity of 1017 mAh g^{-1} among S@MoS_2/SGF (734 mAh g^{-1}), S@Mo_1/SGF (616 mAh g^{-1}), and S@SGF (522 mAh g^{-1}). The first capacity of S@Mo_1/SGF is higher than that of S@SGF (522 mAh g^{-1}), suggesting that the atomically dispersed Mo can improve electrochemical performance. It is noted that the initial capacity of S@MoS_2-Mo_1/SGF (1017 mAh g^{-1}) is much higher than that of S@MoS_2/SGF (734 mAh g^{-1}) and S@Mo_1/SGF (616 mAh g^{-1}). The high initial capacity of S@MoS_2-Mo_1/SGF may originate from the delocalized electron interfaces and synergetic effects of the MoS_2 monolayer and Mo_1. Moreover, S@MoS_2-Mo_1/SGF shows the lowest polarization (0.51 V) between discharge and charge curves compared with S@MoS_2/SGF (0.53 V) and S@SGF (0.58 V). Nyquist plots for S@MoS_2-Mo_1/SGF, S@MoS_2/SGF, and S@SGF in Figure S14 (Supporting Information) indicate that the integrated MoS_2-Mo_1 with electron delocalization can improve the conductivity of sulfur.

Figure 3c shows S@MoS_2-Mo_1/SGF possesses the best reversible capacity of 1042, 831, 529, 281, and 171 mAh g^{-1} at current densities of 0.2, 0.5, 1, 2, and 5 A g^{-1}, respectively (Figure 3c). The capacity of S@MoS_2-Mo_1/SGF can recover to 768 mAh g^{-1} when the current density is returned to 0.1 A g^{-1}, which is much higher than S@MoS_2/SGF (550 mAh g^{-1}) and S@SGF (394 mAh g^{-1}). The initial Coulombic efficiency (CE) of S@MoS_2-Mo_1/SGF (55.2%) is also higher than S@MoS_2/SGF (47.6%) and S@SGF (45.2%). Figure 3d displays the cyclic stability of S@MoS_2-Mo_1/SGF, S@MoS_2/SGF, and S@SGF electrode samples with their CEs at 0.1 A g^{-1}. A capacity of 505 mAh g^{-1} can be maintained after 1000 cycles for the S@MoS_2-Mo_1/SGF cathode, displaying an extremely low capacity fading rate of 0.05% per cycle. In contrast, the S@MoS_2/SGF and S@SGF cathodes maintain only 252 and 159 mAh g^{-1} after 1000 cycles, rendering capacity fade rates of 0.065% and 0.07% per cycle, respectively. The ultralow capacity fading rate of S@MoS_2-Mo_1/SGF is attributed to the constructed electron delocalization interface in atomically dispersed MoS_2-Mo_1, which can provide free electrons to rapidly reduce polysulfides into the final product Na_2S. S@MoS_2-Mo_1/SGF cathode was also evaluated at high current density (Figure 3c) and high sulfur loading (Figure S15, Supporting Information), which usually requires

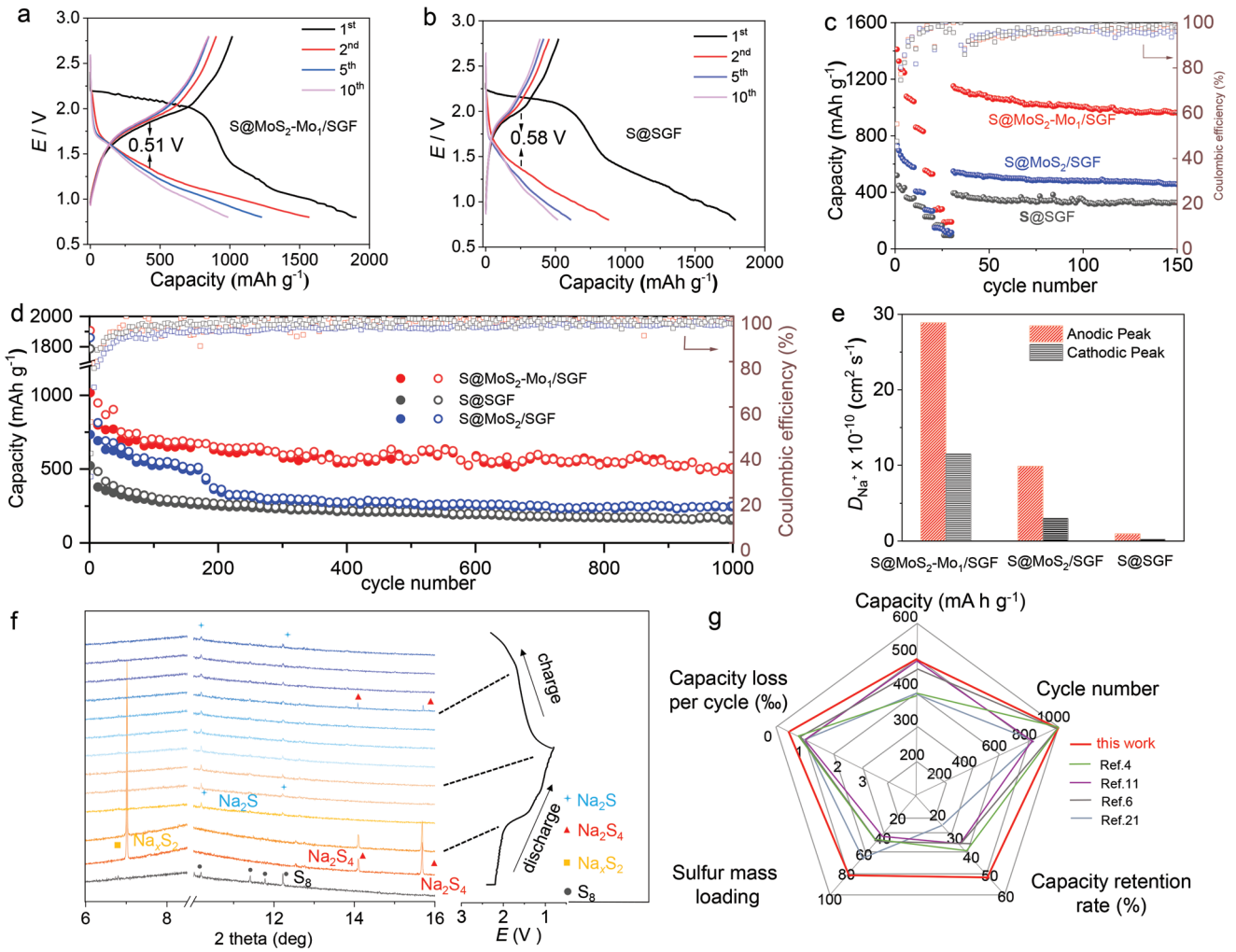

Figure 3. RT-Na/S batteries performance. Discharge/charge curves of a) S@MoS_2-Mo_1/SGF, and b) S@SGF at 100 mA g^{-1}. c) rate performance, d) cycle performance and e) Na^+ ion diffusion coefficients for S@MoS_2-Mo_1/SGF, S@MoS_2/SGF, and S@SGF. f) In situ synchrotron XRD of a S@MoS_2-Mo_1/SGF cathode, corresponding with the initial galvanostatic charge/discharge curves at 0.5 A g^{-1}. g) Cell performance comparison between a S@MoS_2-Mo_1/SGF cathode and previously reported literatures.

faster redox kinetics of polysulfide conversion. Notably, the S@MoS_2-Mo_1/SGF shows the best cycling performance with the highest sulfur capacity among all the reported works (Figure 3g; Table S1, Supporting Information). To investigate the kinetic conversion of polysulfides and Na_2S, cyclic voltammograms (CVs) for S@MoS_2-Mo_1/SGF, S@MoS_2/SGF, and S@SGF at various scan rates (v) were carried out (Figures S16–S18, Supporting Information). Clear-cut anodic and cathodic peaks were selected to investigate Na^+ ion diffusion coefficients (D_{Na+}) based on the Randles–Sevcik equation.[23] Figure 3e shows that the anodic D_{Na+} of S@MoS_2-Mo_1/SGF is 2.89 × 10^{-9} cm^2 s^{-1}, which is 2.93 and 30 times higher than those of S@MoS_2/SGF (9.87 × 10^{-11} cm^2 s^{-1}) and S@SGF (9.56 × 10^{-12} cm^2 s^{-1}), respectively. The D_{Na+} of S@MoS_2-Mo_1/SGF is the largest, demonstrating the kinetic conversion of sodium polysulfides into Na_2S is the fastest. It is well-known that MoS_2 undergoes different reaction mechanisms at various voltages: intercalation type from ≈0.75 to 1.0 and conversion mechanisms below 0.75 V.[24] It can be clearly seen that S@MoS_2-Mo_1/SGF and S@MoS_2/SGF present a cathodic peak at ≈0.82 V and an anodic peak at ≈1.51 V (Figures S15 and S16, Supporting Information), which could be attributed to the sodiation/desodiation of MoS_2. The formation of Na_xMoS_2 also could enhance the reactivity of Na_2S,[24] thus improving its conversion kinetics.

The in situ synchrotron XRD (λ = 0.5904 Å) was performed to reveal the sodium-storage mechanism of S@MoS_2-Mo_1/SGF cathodes (Figure 3f). The initial peaks at ≈10.18°, 11.41°, 11.78°, and 12.26° are attributed to the four (222), (026), (311), and (040) planes of sulfur (JCPDF no.08–0247), which correspond to the four XRD peaks in Figure S11 (Supporting Information). Then, the three new peaks at 7.01°, 14.09°, and 15.69° evolve upon discharge to 2.0 V. The peak at 7.01° could be attributed to the long chain polysulfides (Na_2S_x, $4 < x \leq 8$)[25], while the 14.09° and 15.69° peaks are assigned to the (213) and (312) planes of Na_2S_4 (JCPDF no. 71–0516), respectively.[22] When the cell was further discharged to 1.3 V, the above three peaks disappeared and two new peaks at ≈10.20° and 12.22° arise. These two new peaks are ascribed to the (111) and (200) planes of Na_2S (JCPDF

no. 23–0441). When the S@MoS_2-Mo_1/SGF cell discharged to ≈0.82 V, the XRD signal of Na_xMoS_2 was not detected, which may be assigned to the low mass loading of Mo (≈1.2 wt.%), in agreement with the absence of XRD peaks of MoS_2 in Figure S11 (Supporting Information). The absence of Na_2S_3 and Na_2S_2 suggests that any Na_2S_4 is quickly reduced into the final product Na_2S. The discharge process is illustrated in the following Equations (1)–(2)

$$S \rightarrow Na_2S_x \rightarrow Na_2S_4 \rightarrow Na_2S \quad (1)$$

$$Mo\,/\,MoS_2 \rightarrow Na_xMoS_2 \quad (2)$$

When the cell is further charged to ≈1.8 V, the signal of Na_2S_4 can be detected. But, the Na_2S_x peak (7.01°) and S peaks are undetected, suggesting its high conversion kinetics. In addition, the Na_2S peak still can be detected after the first charge process due to its partial reversibility. This accumulated Na_2S is the main reason of the capacity fading of S@MoS_2-Mo_1/SGF. Conversely, the charging process can be described as:

$$Na_2S \rightarrow Na_2S_4 \rightarrow Na_2S_x \rightarrow S \quad (3)$$

$$Na_xMoS_2 \rightarrow Mo\,/\,MoS_2 \quad (4)$$

Therefore, the conversion process from Na_2S to Na_2S_4 is fast and highly reversible, thereby resulting in excellent cyclability and rate performance. The chemical adsorption ability of these materials for polysulfides was also evaluated by exposing Na_2S_6 to MoS_2-Mo_1/SGF and SGF (Figure S19, Supporting Information). The color of clear solutions exposed to S@MoS_2-Mo_1/SGF is changed from brown to almost colorless after 24 h. In contrast, clear solutions exposed to S@SGF remained a steady brown color. These findings indicate that MoS_2-Mo_1/SGF demonstrates efficient confinement of Na_2S_6 and outstanding capability to electrocatalytically transform Na_2S_6 into the final Na_2S.

2.3. Mechanistic Investigation of the Sulfur Cathodes in RT-Na/S Batteries

Density functional calculations were performed to investigate the origin of the excellent electrochemical catalytic performance of MoS_2-Mo_1/SGF. According to different chemical valences and coordination environments, the electron orbitals of Molybdenum can be roughly divided into three categories. Molybdenum in MoS_2 is embodied in the +4 valence state with the $[Kr]4d^05s^2$ atomic orbital, while ideally metallic Molybdenum presents a 0 valence state, and the atomic orbital is $[Kr]4d^55s^1$ (It is worth noting that the orbital distribution at this time tends to be the half-full distribution of d orbitals according to Hund's rule). In another case, Molybdenum displays +1 to +3 valence state in the unsaturated coordination environment (Mo_xS_2) (in the junction between MoS_2 and Pure Mo). Here, Mo^{2+} with the atomic orbital of $[Kr]4d^25s^2$ is selected as the model for Mo_xS_2. For Na_2S adsorption, the negative coordination ion is S^{2-}, where the atomic orbital is $[Ne]3s3p^6$. According to Molecular Orbital (MO) theory, the 4d electron in Molybdenum and the 3p electron in Sulfur will form a linear combination of atomic orbitals. They divide into bonding and antibonding orbitals, which can strengthen or weaken the chemical bond respectively. As shown in **Figure 4**a, Mo^0 possesses extra electrons in antibonding orbitals, which would decrease the adsorption strength of Na_2S. Mo^{4+} without d orbital electrons results in the adsorption of Na_2S intermediates being too weak. Different from Mo^0 and Mo^{4+}, Mo^{2+} have electrons in the bonding orbital, and eventually attains the strongest adsorption efficiency. The strong adsorption properties of Mo^{2+} can greatly affect the electrochemical efficiency of RT-Na/S batteries from two aspects. When the intermediates such as Na_2S_4 are adsorbed during the discharge process, the one with stronger adsorption capacity leads to the whole discharge process starting more easily. On the other hand, as the Na atoms have more empty orbitals in Na_2S than Na_2S_4, they may form more covalent bonds when Na_2S is adsorbed. A configuration with good adsorption capacity will lead to a more stable Na_2S adsorption structure on Na_2S*S@MoS_2-Mo_1/SGF than Na_2S_4*S@MoS_2-Mo_1/SGF.

To be consistent with the experimental environment, S@MoS_2-Mo_1/SGF was simulated by a couple of Mo single atom regions (Figure S20a, Supporting Information, blue balls), MoS_2 layer parts (Figure S20a, Supporting Information, violet balls), and interfaces (Figure S20a, Supporting Information, green balls). All these units and the graphene substrate form a complete S@MoS_2-Mo_1/SGF model (FigureS20b, Supporting Information). We also selected the isolated graphene in Figure S20c (Supporting Information) as a reference structure. Figures S21–S23 (Supporting Information) present the charge density difference on the interfaces of S@MoS_2-Mo_1/SGF and S@ MoS_2/SGF. Compared with S@MoS_2/SGF, the atomically-dispersed MoS_2-Mo_1 interfaces on S@MoS_2-Mo_1/SGF are accompanied by a significant charge transfer. The *d*-band centers (E_d) obtained from the corresponding calculated partial density of state (PDOS) of S@MoS_2-Mo_1/SGF and S@MoS_2/SGF are depicted in Figure 4b and Figure S24 (Supporting Information). Obviously, layered MoS_2 on S@MoS_2-Mo_1/SGF and S@MoS_2/SGF share a uniform E_d value of –0.52 eV. Nevertheless, the E_d value of Mo single atom for S@MoS_2-Mo_1/SGF shifts to –0.41 eV compared with S@Mo_1/SGF (–0.73 eV), suggesting an enhanced catalytic activity.

Next, we calculated the energy change diagram from Na_2S_4 to Na_2S intermediates based on the three models to simulate the discharge process of RT-Na/S batteries (Figure 4c and Figure S25, Supporting Information). The adsorption energies of Na_2S_4, Na_2S_3, Na_2S_2, and Na_2S on S@MoS_2-Mo_1/SGF are –4.67, –8.66, –10.66, and –14.66 eV, respectively, which suggests S@MoS_2-Mo_1/SGF can smoothly complete the discharging reaction. However, the adsorption energies for the four intermediates on S@MoS_2/SGF are –1.37, –3.57, –2.48, and –1.14 eV, respectively. And, the adsorption energies of the four intermediates on SGF are –1.71, –0.81, 1.13, and 4.05 eV, implying that the discharge process cannot pass the first intermediate of Na_2S_4.

It is well-established that the energy change diagram only reflects the simulation of the adsorption process under ideal conditions. To make the calculation closer to the existing system at room temperature, an ab initio molecular dynamics (AIMD) simulation was carried out (Figure 4d; Figure S26, and Table S2, Supporting Information). After 5 ps of dynamics simulation,

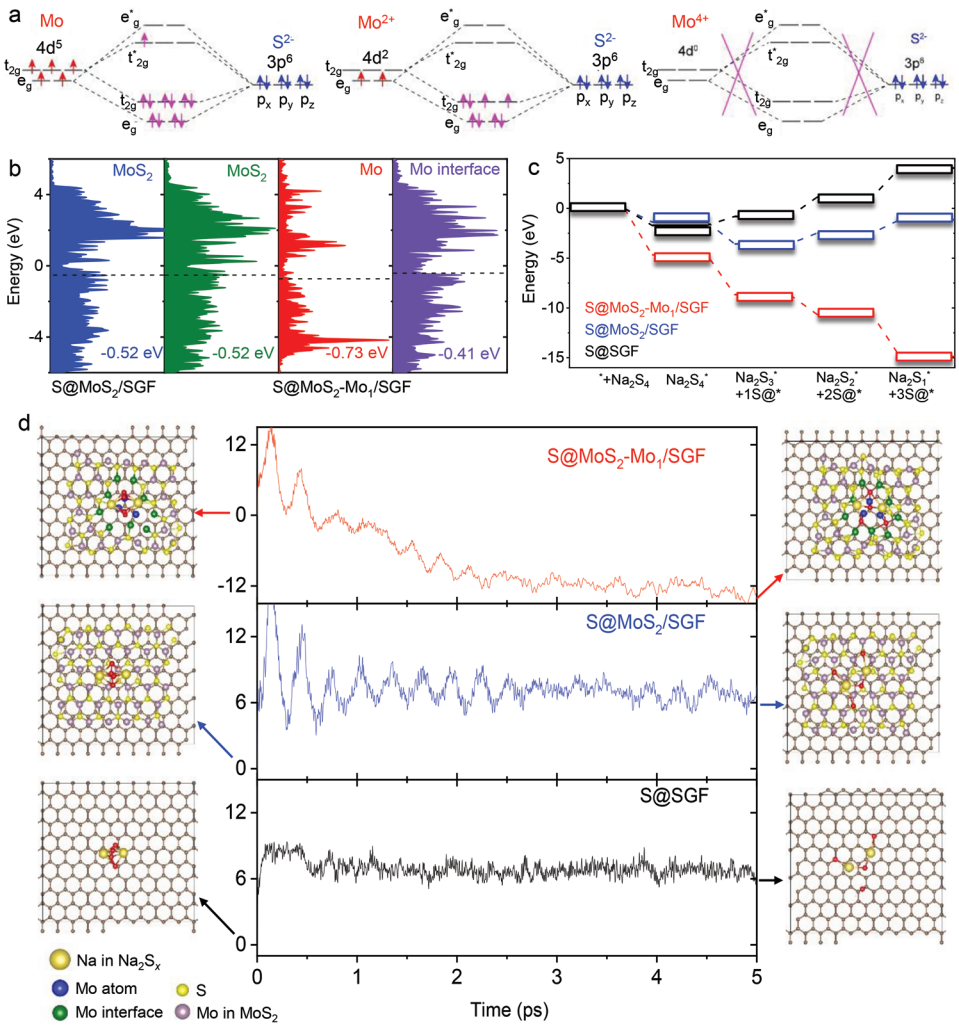

Figure 4. Mechanistic investigation. a) Schematic diagram of molecular orbitals for 4d electrons in Mo and 3p electrons in S elements coordinated at different valences. b) d-band centers on the corresponding active Mo sites of S@MoS_2-Mo_1/SGF and S@MoS_2/SGF. c) Energy change diagram of discharge process from Na_2S_4 to Na_2S intermediates on S@MoS_2-Mo_1/SGF, S@MoS_2/SGF, and SGF. d) Adsorption energies (eV) of Na_2S_4 as a function of ab initio molecular dynamics (AIMD) simulation time on the corresponding sodium–sulfur battery model.

S@MoS_2-Mo_1/SGF was found to have the only large negative adsorption energy (≈–12 eV) among the three models, which is consistent with thermodynamic results. On contrary, S@MoS_2/SGF and SGF would encounter huge positive energy barriers (≈6 eV) to complete the discharge process. We also notice that the final adsorbed state structure of S@MoS_2-Mo_1/SGF is more inclined to the Na_2S intermediate whereas the adsorbed final state structures on S@MoS_2/SGF and SGF are close to Na_2S_3 and Na_2S_4, respectively.

Also, the migration of sodium ions in the three models was studied by computational analysis (**Figure 5**a–c). We performed calculations of the formation energies of the sodium ions on different sites (as shown in Figure S27 and Table S2, Supporting Information). The largest possible reaction path was chosen and shown in Figure 5d,e. It is clear that, in either direction, the order of energy barriers is MoS_2-Mo_1/SGF(0.02/0.20) < S@MoS_2/SGF(0.57/0.70) < SGF(1.61/1.61). According to the Arrhenius theorem, these results demonstrate the migration rate order of sodium ions as follows: MoS_2-Mo_1/SGF > S@MoS_2/SGF > SGF, which is consistent with our experimental observations.

3. Conclusion

In summary, S@MoS_2-Mo_1/SGF material with atomic-level dual-active sites has been synthesized as a superior sulfur host for cathodes in RT-Na/S batteries. The atomically dispersed dual-active sites with their unique coordination environment produce delocalized electrons, which can provide free electrons to sulfur and thus efficiently improve the reactivity of sulfur and the kinetic conversion of polysulfides. The S@MoS_2-Mo_1/SGF material exhibits an unprecedented reversible capacity of 505 mAh g^{-1} over 1000 cycles with a low capacity fading rate of 0.05% per cycle. A series of experimental characterizations and computational calculations reveal that the excellent performance of S@MoS_2-Mo_1/SGF can be attributed to the created layered MoS_2-Mo_1 sites, which can optimize the adsorption

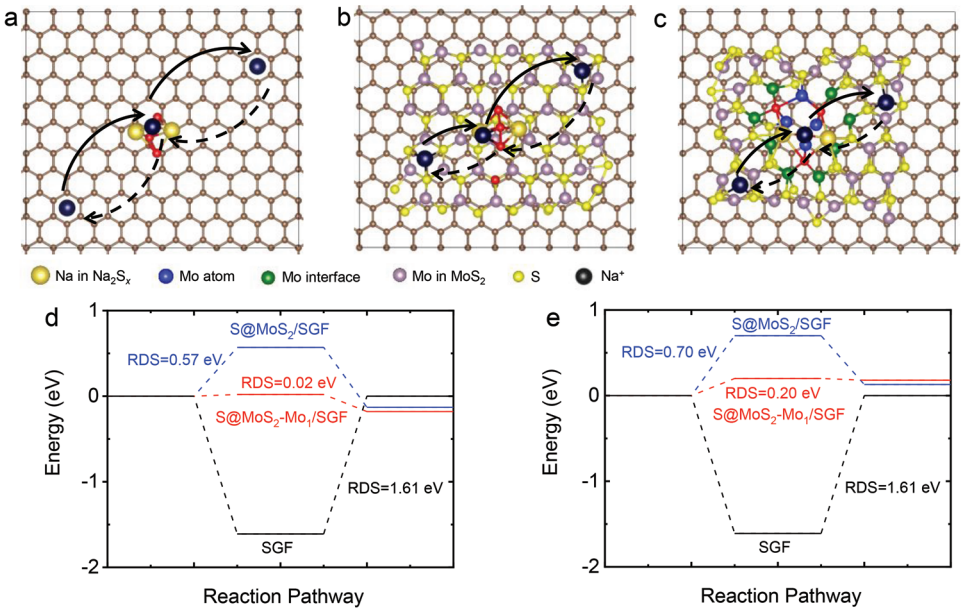

Figure 5. Sodium ions migrating on sulfur hosts. Sodium ion migration pathway in a) Na_2S_4*SGF, b) Na_2S_3*S@MoS_2/SGF, c) Na_2S_1*S@MoS_2-Mo_1/SGF. The number of sulfur is derived from the most stable adsorbate from previous thermodynamic calculations for the corresponding structure calculated energy barriers of sodium ions migration barriers in d) solid and e) dashed line directions.

energy of the intermediates and spontaneously decompose polysulfides into Na_2S.

4. Experimental Section

Synthesis of Sulfur Cathode Materials: Mo_1/SGF was synthesized by the previously reported templated pyrolysis.[17] The mass loading of Mo was ≈6.9 wt.%, determined by inductively coupled plasma optical emission spectroscopy (ICP-OES). The S@MoS_2-Mo_1/SGF was synthesized as follows: a mixture of Mo_1/SGF:S (mass ratio of 1:9) was grounded by mortar and sealed in a quartz ampoule, then thermally treated at 300 °C for 12 h. The Mo mass loading of S@MoS_2-Mo_1/SGF was ≈1.2 wt.%, measured by ICP-OES. The synthesis procedure of S@MoS_2/SGF was the same as S@MoS_2-Mo_1/SGF but the thermal treatment was extended to 24 h. To prepare the S@SGF, pure SGF was used to replace Mo_1/SGF. S@Mo_1/SGF was prepared by pyrolyzing the mixture of Mo_1/SGF and S at 155 °C for 12 h.

Structural Characterization: The morphologies of these sulfur samples were obtained by using transmission electron microscopy (TEM, JEOL 2011, 200 keV) and scanning TEM (STEM, JEOL ARM–200F, 200 keV). The X-ray diffraction (XRD) patterns were obtained using powder XRD (GBC MMA diffractometer) with Cu Kα radiation at a scan rate of 1° min^{-1}. X-ray photoelectron spectroscopy (XPS) was collected by employing Al Kα radiation with a fixed analyzer transmission mode. The XAS results were investigated at Mo and S K-edge recorded at the X-ray absorption spectroscopy (XAS) station of the Beijing Synchrotron Radiation Facility (BSRF) in transmission mode for Mo and S K-edge XAFS.

Electrochemical Measurements: Electrochemical tests were carried out by assembling coin cells in an argon-filled glove box. The slurry was prepared by fully mixing 70 wt.% active materials, 20 wt.% carboxymethyl cellulose (CMC), and 10 wt.% carbon black with an amount of water in a planetary mixer (KK-250S). The weight percentages of sulfur in S@MoS_2-Mo_1/SGF, S@MoS_2/SGF, and S@SGF electrodes were determined to be 57.7, 47.6, and 38.0 wt.%, respectively. The obtained slurry was pasted on Cu-foil using a doctor-blade with a thickness of 100 µm, followed by drying at 80 °C in a vacuum oven overnight. The working electrode was prepared by punching the electrode film into discs with a 0.97 cm diameter. The area mass loading of pure sulfur on S@MoS_2-Mo_1/SGF, S@MoS_2/SGF, and S@SGF electrodes was ≈0.96, 1.09, and 1.21 mg cm^{-2}, respectively. All the capacities of cells were normalized based on the mass of sulfur. Sodium foil was employed as both reference and counter electrode. The electrodes in test cells were separated by a glass-fiber separator. An electrolyte consisting of 1.0 M $NaClO_4$ in propylene carbonate/ethylene carbonate with a volume ratio of 1:1 and 5 wt.% fluoroethylene carbonate additive (PC/EC + 5wt.% FEC) were prepared. The electrochemical performance was tested on a LAND Battery Tester with a voltage window of 0.8 to 2.8 V. The minimum voltage to estimate the reversible capacity was 0.8 V. The ratio of electrolyte to sulfur in composites was 10 mL g^{-1}. Cyclic voltammetry was performed using a Biologic VMP-3 electrochemical workstation.

Computational Methods: The density-functional theory (DFT)[26] calculations were performed with the Vienna Ab initio Simulation Package (VASP)[27] codes 5.4. The PAW[28] pseudo-potentials and the Perdew–Burke–Ernzerhof[29] exchange-correlation functional and a plane wave cutoff of 500 eV were used in the calculations. Gamma *k*-point mesh was sampled for all models. Spin-polarized calculations were identified for all surfaces, and the convergence of energy and force was set to 10^{-4} eV and 0.05 eV $Å^{-1}$. The DFT-D3 method[30] was adopted to consider van der Waals corrections. For AIMD simulations, five ps studies (2500 steps, two fs per step) within the canonical (NVT) ensemble at 300 K to accelerate the dissociation rate of the Na_2S_4 cluster on the corresponding structures were performed.

Supporting Information

Supporting Information is available from the Wiley Online Library or from the author.

Acknowledgements

B.Z. and L.C. contributed equally to this work. S.Z. thanks the Australian Research Council for financial support from the Discovery Early Career Researcher Award (DE220100676) and Discovery Project (DP220101511).

This research was supported by the National Natural Science Foundation of China (22279011), Fundamental Research Funds for the Central Universities (Grant No. 2022CDJXY-003), the Ministry of Science and Technology of China (No. 2017YFA0204904), and Australian Research Council (DE220101113). The numerical calculations in this paper were completed on the supercomputing system in the Supercomputing Center of the University of Science and Technology of China. The authors acknowledge Dr. Stephen Bewlay for his critical reading.

Open access publishing facilitated by The University of Sydney, as part of the Wiley - The University of Sydney agreement via the Council of Australian University Librarians.

Conflict of Interest

The authors declare no conflict of interest.

Data Availability Statement

The data that support the findings of this study are available from the corresponding author upon reasonable request.

Keywords

dual-site cathodes, monolayer clusters, sodium sulfur batteries, single atom, sulfur electrodes

Received: July 27, 2022
Revised: October 26, 2022
Published online: November 29, 2022

[1] a) C. Wu, Y. Lei, L. Simonelli, D. Tonti, A. Black, X. Lu, W.-H. Lai, X. Cai, Y.-X. Wang, Q. Gu, S.-L. Chou, H.-K. Liu, G. Wang, S.-X. Dou, *Adv. Mater.* **2022**, *34*, 2108363; b) C. Zhao, G.-L. Xu, Z. Yu, L. Zhang, I. Hwang, Y.-X. Mo, Y. Ren, L. Cheng, C.-J. Sun, Y. Ren, X. Zuo, J.-T. Li, S.-G. Sun, K. Amine, T. Zhao, *Nat. Nanotechnol.* **2021**, *16*, 166; c) L. Peng, Z. Wei, C. Wan, J. Li, Z. Chen, D. Zhu, D. Baumann, H. Liu, C. S. Allen, X. Xu, A. I. Kirkland, I. Shakir, Z. Almutairi, S. Tolbert, B. Dunn, Y. Huang, P. Sautet, X. Duan, *Nat. Catal.* **2020**, *3*, 762.

[2] a) Y. Lei, C. Wu, X. Lu, W. Hua, S. Li, Y. Liang, H. Liu, W.-H. Lai, Q. Gu, X. Cai, N. Wang, Y.-X. Wang, S.-L. Chou, H.-K. Liu, G. Wang, S.-X. Dou, *Angew. Chem., Int. Ed.* **2022**, *61*, e202200384; b) D. Cao, X. Shen, A. Wang, F. Yu, Y. Wu, S. Shi, S. A. Freunberger, Y. Chen, *Nat. Catal.* **2022**, *5*, 193.

[3] a) X. Ye, J. Ruan, Y. Pang, J. Yang, Y. Liu, Y. Huang, S. Zheng, *ACS Nano* **2021**, *15*, 5639; b) C. Ye, H. Jin, J. Shan, Y. Jiao, H. Li, Q. Gu, K. Davey, H. Wang, S.-Z. Qiao, *Nat. Commun.* **2021**, *12*, 7195; c) W. Bao, R. Wang, C. Qian, Z. Zhang, R. Wu, Y. Zhang, F. Liu, J. Li, G. Wang, *ACS Nano* **2021**, *15*, 16207.

[4] a) D. Zhou, X. Tang, X. Guo, P. Li, D. Shanmukaraj, H. Liu, X. Gao, Y. Wang, T. Rojo, M. Armand, G. Wang, *Angew. Chem., Int. Ed.* **2020**, *59*, 16725; b) S.-H. Chung, A. Manthiram, *Adv. Mater.* **2019**, *31*, 1901125.

[5] a) X. Zhou, Z. Yu, Y. Yao, Y. Jiang, X. Rui, J. Liu, Y. Yu, *Adv. Mater.* **2022**, *34*, 2200479; b) J. Zhou, Y. Yang, Y. Zhang, S. Duan, X. Zhou, W. Sun, S. Xu, *Angew. Chem., Int. Ed.* **2021**, *60*, 10129.

[6] a) X.-Q. Zhang, Q. Jin, Y.-L. Nan, L.-P. Hou, B.-Q. Li, X. Chen, Z.-H. Jin, X.-T. Zhang, J.-Q. Huang, Q. Zhang, *Angew. Chem., Int. Ed.* **2021**, *60*, 15503; b) H. Chen, G. Zhou, D. Boyle, J. Wan, H. Wang, D. Lin, D. Mackanic, Z. Zhang, S. C. Kim, H. R. Lee, H. Wang, W. Huang, Y. Ye, Y. Cui, *Matter* **2020**, *2*, 1605; c) Q. Pang, A. Shyamsunder, B. Narayanan, C. Y. Kwok, L. A. Curtiss, L. F. Nazar, *Nat. Energy* **2018**, *3*, 783; d) H. Ye, L. Ma, Y. Zhou, L. Wang, N. Han, F. Zhao, J. Deng, T. Wu, Y. Li, J. Lu, *Proc. Natl. Acad. Sci. USA* **2017**, *114*, 13091; e) Y.-X. Wang, B. Zhang, W. Lai, Y. Xu, S.-L. Chou, H.-K. Liu, S.-X. Dou, *Adv. Energy Mater.* **2017**, *7*, 1602829; f) Q. Lu, X. Wang, J. Cao, C. Chen, K. Chen, Z. Zhao, Z. Niu, J. Chen, *Energy Stor. Mater.* **2017**, *8*, 77.

[7] a) A. Ghosh, S. Shukla, M. Monisha, A. Kumar, B. Lochab, S. Mitra, *ACS Energy Lett.* **2017**, *2*, 2478; b) X. Yu, A. Manthiram, *Chem. Mater.* **2016**, *28*, 896; c) Z. Yan, Y. Liang, J. Xiao, W. Lai, W. Wang, Q. Xia, Y. Wang, Q. Gu, H. Lu, S.-L. Chou, Y. Liu, H. Liu, S.-X. Dou, *Adv. Mater.* **2020**, *32*, 1906700.

[8] a) S. Xin, Y. X. Yin, Y. G. Guo, L. J. Wan, *Adv. Mater.* **2014**, *26*, 1261; b) S. Zhang, Y. Yao, Y. Yu, *ACS Energy Lett.* **2021**, *6*, 529.

[9] a) Z. Yan, J. Xiao, W. Lai, L. Wang, F. Gebert, Y. Wang, Q. Gu, H. Liu, S.-L. Chou, H. Liu, S.-X. Dou, *Nat. Commun.* **2019**, *10*, 4793; b) L. Wang, T. Wang, L. Peng, Y. Wang, M. Zhang, J. Zhou, M. Chen, J. Cao, H. Fei, X. Duan, J. Zhu, X. Duan, *Natl. Sci. Rev.* **2022**, *9*, nwab050.

[10] a) B.-W. Zhang, T. Sheng, Y.-D. Liu, Y.-X. Wang, L. Zhang, W.-H. Lai, L. Wang, J. Yang, Q.-F. Gu, S.-L. Chou, H.-K. Liu, S.-X. Dou, *Nat. Commun.* **2018**, *9*, 4082; b) B.-W. Zhang, T. Sheng, Y.-X. Wang, S. Chou, K. Davey, S.-X. Dou, S.-Z. Qiao, *Angew. Chem., Int. Ed.* **2019**, *58*, 1484.

[11] H. Yang, B. Zhang, Y.-X. Wang, K. Konstantinov, H.-K. Liu, S.-X. Dou, *Adv. Energy Mater.* **2020**, *10*, 2001764.

[12] a) Z. Yang, R. Xiao, X. Zhang, X. Wang, D. Zhang, Z. Sun, F. Li, *Energy Environ. Mater.* **2022**, *5*, 693; b) S.-C. Wu, Y.-H. Huang, C.-R. Liao, S.-Y. Tang, T.-Y. Yang, Y.-C. Wang, Y.-J. Yu, T.-P. Perng, Y.-L. Chueh, *Nano Energy* **2021**, *90*, 106590.

[13] a) C. Lu, R. Fang, X. Chen, *Adv. Mater.* **2020**, *32*, 1906548; b) B.-W. Zhang, Y.-X. Wang, S.-L. Chou, H.-K. Liu, S.-X. Dou, *Small Methods* **2019**, *3*, 1800497; c) Y. Yao, S. Hu, W. Chen, Z.-Q. Huang, W. Wei, T. Yao, R. Liu, K. Zang, X. Wang, G. Wu, W. Yuan, T. Yuan, B. Zhu, W. Liu, Z. Li, D. He, Z. Xue, Y. Wang, X. Zheng, J. Dong, C.-R. Chang, Y. Chen, X. Hong, J. Luo, S. Wei, W.-X. Li, P. Strasser, Y. Wu, Y. Li, *Nat. Catal.* **2019**, *2*, 304. d) Z. Zhou, Y. Kong, H. Tan, Q. Huang, C. Wang, Z. Pei, H. Wang, Y. Liu, Y. Wang, S. Li, X. Liao, W. Yan, S. Zhao, *Adv. Mater.* **2022**, *34*, 2106541. e) Z. Wang, J. Huang, L. Wang, Y. Liu, W. Liu, S. Zhao, Z.-Q. Liu, *Angew. Chem., Int. Ed.* **2022**, *61*, e202114696.

[14] a) K. Johnson, D. Weix, *Science* **2019**, *363*, 819; b) S. Zhao, C. Tan, C.-T. He, P. An, F. Xie, S. Jiang, Y. Zhu, K.-H. Wu, B. Zhang, H. Li, J. Zhang, Y. Chen, S. Liu, J. Dong, Z. Tang, *Nat. Energy* **2020**; c) B.-W. Zhang, L. Ren, Y.-X. Wang, Y. Du, L. Jiang, S.-X. Dou, *Sci. China Mater* **2019**, *62*, 149; d) B.-W. Zhang, L. Ren, Z.-F. Xu, N.-Y. Cheng, W.-H. Lai, L. Zhang, W. Hao, S.-Q. Chu, Y.-X. Wang, Y. Du, L. Jiang, H.-K. Liu, S.-X. Dou, *Small* **2021**, *17*, 2100732.

[15] a) S. Lopatin, A. Aljarb, V. Roddatis, T. Meyer, Y. Wan, J.-H. Fu, M. Hedhili, Y. Han, L.-J. Li, V. Tung, *Sci. Adv.* **2020**, *6*, eabb8431; b) J. Hong, Z. Hu, M. Probert, K. Li, D. Lv, X. Yang, L. Gu, N. Mao, Q. Feng, L. Xie, J. Zhang, D. Wu, Z. Zhang, C. Jin, W. Ji, X. Zhang, J. Yuan, Z. Zhang, *Nat. Commun.* **2015**, *6*, 6293.

[16] P. Kumar, J. P. Horwath, A. C. Foucher, C. C. Price, N. Acero, V. B. Shenoy, E. A. Stach, D. Jariwala, *npj 2D Mater. Appl.* **2020**, *4*, 16.

[17] C. Tang, Y. Jiao, B. Shi, J.-N. Liu, Z. Xie, X. Chen, Q. Zhang, S.-Z. Qiao, *Angew. Chem., Int. Ed.* **2020**, *59*, 9171.

[18] B.-W. Zhang, S. Li, H.-L. Yang, X. Liang, W.-H. Lai, S. Zhao, J. Dong, S.-Q. Chu, Q.-F. Gu, J. Liang, Y. Du, X. Xu, L. Cao, Y.-X. Wang, F. Pan, S.-L. Chou, H.-K. Liu, S.-X. Dou, *Cell Rep. Phys. Sci.* **2021**, *2*, 100531.

[19] B. Lassalle-Kaiser, D. Merki, H. Vrubel, S. Gul, V. K. Yachandra, X. Hu, J. Yano, *J. Am. Chem. Soc.* **2015**, *137*, 314.
[20] L. Wu, A. Longo, N. Y. Dzade, A. Sharma, M. M. R. M. Hendrix, A. A. Bol, N. H. de Leeuw, E. J. M. Hensen, J. P. Hofmann, *ChemSusChem* **2019**, *12*, 4383.
[21] C. Ye, Y. Jiao, D. Chao, T. Ling, J. Shan, B. Zhang, Q. Gu, K. Davey, H. Wang, S.-Z. Qiao, *Adv. Mater.* **2020**, *32*, 1907557.
[22] B. Chen, T. Wang, S. Zhao, J. Tan, N. Zhao, S. P. Jiang, Q. Zhang, G. Zhou, H.-M. Cheng, *Adv. Mater.* **2021**, *33*, 2007090.
[23] a) L. Wang, X. Chen, S. Li, J. Yang, Y. Sun, L. Peng, B. Shan, J. Xie, *J. Mater. Chem. A* **2019**, *7*, 12732; b) H. Kim, J. Lee, H. Ahn, O. Kim, M. J. Park, *Nat. Commun.* **2015**, *6*, 7278.
[24] Y. Wang, Y. Lai, J. Chu, Z. Yan, Y.-X. Wang, S.-L. Chou, H.-K. Liu, S. X. Dou, X. Ai, H. Yang, Y. Cao, *Adv. Mater.* **2021**, *33*, 2100229.
[25] Y. X. Wang, J. Yang, W. Lai, S. L. Chou, Q. F. Gu, H. K. Liu, D. Zhao, S. X. Dou, *J. Am. Chem. Soc.* **2016**, *138*, 16576.
[26] a) P. Hohenberg, W. Kohn, *Phys. Rev.* **1964**, *136*, B864; b) W. Kohn, L. J. Sham, *Phys. Rev.* **1965**, *140*, A1133.
[27] G. Kresse, J. Furthmuller, *Phys. Rev. B* **1996**, *54*, 11169.
[28] a) P. E. Blochl, *Phys. Rev. B* **1994**, *50*, 17953; b) G. Kresse, D. Joubert, *Phys. Rev. B* **1999**, *59*, 1758.
[29] J. P. Perdew, K. Burke, M. Ernzerhof, *Phys. Rev. Lett.* **1996**, *77*, 3865.
[30] a) S. Grimme, S. Ehrlich, L. Goerigk, *J. Comput. Chem.* **2011**, *32*, 1456; b) J. Moellmann, S. Grimme, *J. Phys. Chem. C* **2014**, *118*, 7615.